Cement and Concrete Research 162 (2022) 106965

Contents lists available at ScienceDirect

Cement and Concrete Research

journal homepage: www.elsevier.com/locate/cemconres

A potential C-S-H nucleation mechanism: atomistic simulations of the portlandite to C-S-H transformation

Xabier M. Aretxabaleta [a,*], Jon López-Zorrilla [a], Christophe Labbez [b], Iñigo Etxebarria [a,c], Hegoi Manzano [a]

[a] Fisika saila, Euskal Herriko Unibertsitatea UPV/EHU, Sarriena Auzoa z/g, 48940 Leioa, Basque Country, Spain
[b] ICB, UMR 6303 CNRS, Univ. Bourgogne Franche-Comté, FR-21000, Dijon, France
[c] EHU Quantum Center, Euskal Herriko Unibertsitatea, UPV/EHU, Spain

ARTICLE INFO

Keywords:
Calcium Silicate Hydrate
Portlandite
Atomistic simulation
Nucleation
Free energy of reaction

ABSTRACT

The nucleation of the C-S-H gel is a complex process, key to controlling the hydration kinetics and microstructure development of cement. In this paper, a mechanism for the crystallization step during the C-S-H gel non-classical nucleation is proposed and explored by atomistic simulation methods. In the proposed mechanism portlandite precursor monolayers undergo a chemically induced transformation by condensation of silicate dimmers, forming C-S-H monolayers. We studied by DFT and nudged elastic band the structural transformation from bulk portlandite to a tobermorite-like calcium hydroxide polymorph, and the silicate condensation reaction at portlandite surface. Then, both processes are studied together, investigating the topochemical transformation from a portlandite monolayer to a C-S-H monolayer at room conditions using targeted molecular dynamics and umbrella sampling methods. Comparing the free energy of the process with thermodynamic data we conclude that the proposed mechanism is a potential path for C-S-H formation.

1. Introduction

Cement is the most manufactured product in the world, with an annual production of more than four thousand million tons in 2020 [1,2]. Because of its massive production, the required energy and generated CO_2 emissions are of vital interest from both an economic and environmental point of view [3]. The hydration of cement results in the formation of hydrates, upon which Calcium Silicate Hydrate (C-S-H) is the main binding phase. The formation and densification of the C-S-H gel drives the setting and hardening of the cement paste. The C-S-H gel has been broadly defined as an amorphous material with variable stoichiometry, usually characterized by its Ca/Si ratio and water content, yet retaining short-range order, forming tobermorite-like structures. Tobermorite is a natural mineral formed by CaO layers sandwiched between infinite Dreieketten silicate chains [4]. In the C-S-H gel, those chains have finite lengths of $3n - 1$ tetrahedra where n is an integer. Two in three silicate tetrahedra share O-O edges with the central CaO layer, while the third one, called bridging site, is oriented to the interlayer space [5,6]. Although silicate dimeric structures are more frequent than longer chains in typical cement conditions, the latter are also formed for low Ca/Si ratio [7].

Unraveling the C-S-H gel nucleation and growth mechanism during hydration is crucial to understanding and eventually controlling the microstructure development and rheology of the cement paste [8]. Scanning electron microscopy (SEM) experiments suggest that the induction and acceleration periods are mainly governed by the heterogeneous nucleation and growth of the C-S-H gel [9,10]. In addition, the growth process is dominated by secondary nucleation of C-S-H particles rather than the growth of primary nuclei [11]. That is to say, the growth of C-S-H takes place where crystals of the species under consideration are already present. For instance, C-S-H seeds have been shown to act directly as secondary nucleation or growth sites for further hydration products, leading the product formation process away from clinker particles [12]. This can be really advantageous from a technological point of view as the nucleation rate can be tuned by the use of additives [13,14].

Regarding the mechanism of C-S-H nucleation, recent experiments using time resolved potentiometry and turbidity together with cryogenic transmission electron microscopy revealed that in a supersaturated solution, synthetic C-S-H follows a non-classical nucleation process consisting of two steps [15]. The authors suggest as a first step that dense liquid regions form "amorphous spheroids" with a diameter of about 50 nm. In a second step, the aggregation of the chemical species within the spheroids leads the system to crystallization

* Corresponding author.
E-mail addresses: xabier.mendez@ehu.eus (X.M. Aretxabaleta), hegoi.manzano@ehu.eus (H. Manzano).

https://doi.org/10.1016/j.cemconres.2022.106965
Received 21 February 2022; Received in revised form 2 August 2022; Accepted 30 August 2022
Available online 18 September 2022

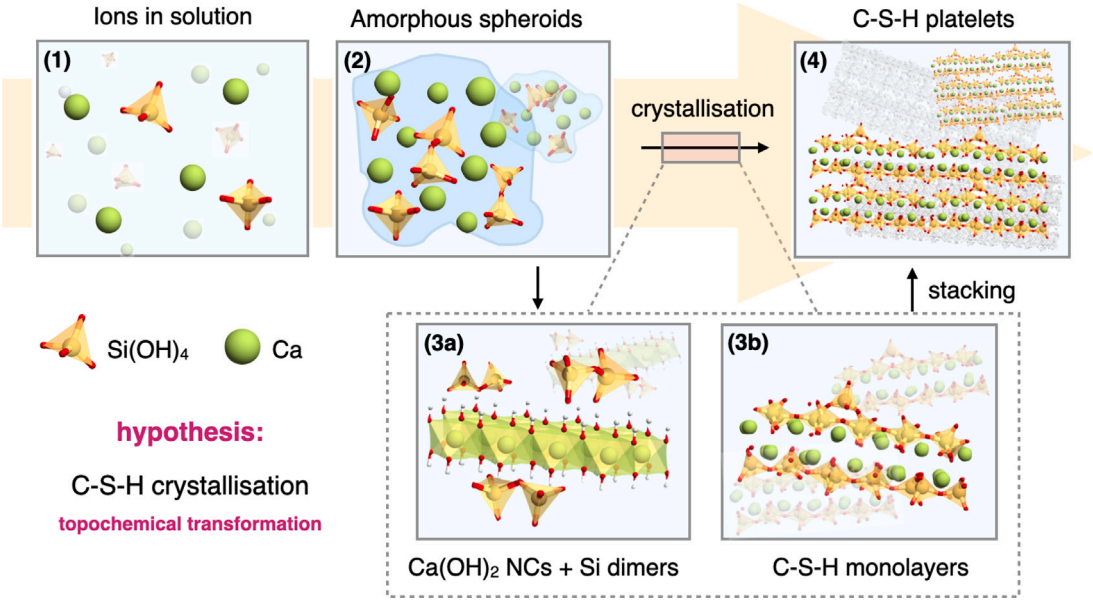

Fig. 1. Proposed mechanism for the early stage formation of C-S-H. Within this model, the ions in solution would create high dense amorphous spheroids which then would form portlandite monolayers surrounded by silicate dimers. Finally, this monolayers would suffer a topochemical phase transformation into a C-S-H monolayer which they would create the final C-S-H by the stacking of them.

into C-S-H. The effects of polycarboxylate superplasticizers on C-S-H nucleation have also been studied using transmission electron microscopy (TEM) and dynamic light scattering leading to similar conclusions [16]. In the framework of modeling, various methodologies have been used to examine the nucleation and growth of C-S-H. On the mesoscale, semi-analytical models like the boundary nucleation and growth (BNG) and microstructure-based kinetics (MBK) have been employed to predict cement's hydration rate [17–20]. On a lower scale, colloidal models based on random sequential addition [21] and rate-dependent creation of colloidal nanoparticles [22] have been used to study the primary nucleation of C-S-H particles and the subsequent growth by secondary nucleation. These models fit with reasonable accuracy the experimental C-S-H hydration rate and give interesting information about the microstructure development, nucleation rates, and percolation thresholds [23,24]. A more detailed "sheet growth model" has also been proposed to study the growth rate and microstructure development [25].

However, none of the above-mentioned models take into account the atomic structure of the nanoparticles. They do not provide insight on the atomic scale nucleation mechanism, which will govern the formation of the nanoparticles or sheets. To that end, atomic-scale simulations can be a very valuable tool, yet few studies on the topic have been reported so far, probably due to the intrinsic time and length scale limitations [26]. Manzano et al. proposed a precursor nanocluster or basic building block based on the structure of tobermorite, and investigated their aggregation by *ab initio* calculations [27]. Very recently, Yang et al. focused on the earliest hydration period and studied the most stable prenucleation species using density functional theory (DFT) [28]. In addition, a series of studies have tried to simulate the process of nucleation by using molecular dynamics at high temperatures [29–31]. However, the obtained particles did not properly represent the atomic structure of the C-S-H gel. That is probably due to the very high temperatures used to facilitate silicate polymerization within the accessible time scale (tens of nanoseconds).

In this work, we take a different approach to investigate the possibility of the crystallization of the C-S-H gel by the means of portlandite nanocluster precursors. The formation of C-S-H as a result of modified portlandite layer by condensation of monomeric silicate anions was proposed as a C-S-H model [32,33]. However, these models were deprecated when the silicate chain structure and tobermorite-like structure was confirmed [34,35]. The importance of portlandite layers in the formation of C-S-H has also been studied and recently it has been proposed that C-S-H is formed by tobermorite layers sandwiched between portlandite layers [36,37]. In spite of these studies and the suggestions made in the literature, the transformation from portlandite to tobermorite layers has never been explicitly studied to the best of our knowledge. As depicted in Fig. 1, we propose a model which takes portlandite nanocluster precursors (consisting of monolayers) as a starting point. These monolayers undergo a chemically induced topochemical transformation by condensation of silicate dimmers in solution, forming C-S-H monolayers. This hypothesis is based on the structural similarity between the M-OH arrangement in the strontium hydroxide crystal and the Ca-O layers in tobermorite shown in Fig. 2. Both layers have a zigzag arrangement with the metal in a seven-fold coordinated site. Since calcium and strontium are isoelectronic, portlandite monolayers could undergo a structural transformation forming $Sr(OH)_2$ like layers. We suggest that this transformation would be induced by the condensation of silica chains creating tobermorite-like monolayers. In fact, recent studies of the C-S-H gel structure using pair distribution functions (PDFs) from synchrotron X-ray powder diffraction suggest that the C-S-H gel is formed by an intimate mixture of clinotobermorite and portlandite layers, at least for Ca/Si > 1.2 [15,36]. This point has been validated by computational methods [38] but is not fully clear, as Kumar et al. reported a controlled synthesis protocol to reach Ca/Si =2 without traces of portlandite [39]. While these experimental studies give very relevant microscopic information about the C-S-H nucleation, the atomic-scale mechanism is still beyond their resolution.

Herein, we study the proposed model in three steps. First, we investigate the structural transformation from bulk portlandite to the $Sr(OH)_2$-like phase, to examine its feasibility using variable nudged elastic band (VC-NEB) together with DFT. Second, we study the silicate condensation mechanism on a portlandite layer using the same methodology. Finally, we investigate the topochemical structural transformation from a portlandite monolayer to a C-S-H monolayer induced by the condensation of silicate dimers at room temperature and pressure. This complex process is studied using targeted molecular dynamics (TMD) and umbrella sampling (US) to obtain structural and thermodynamic information such as internal energy, enthalpy, entropy and free energy.

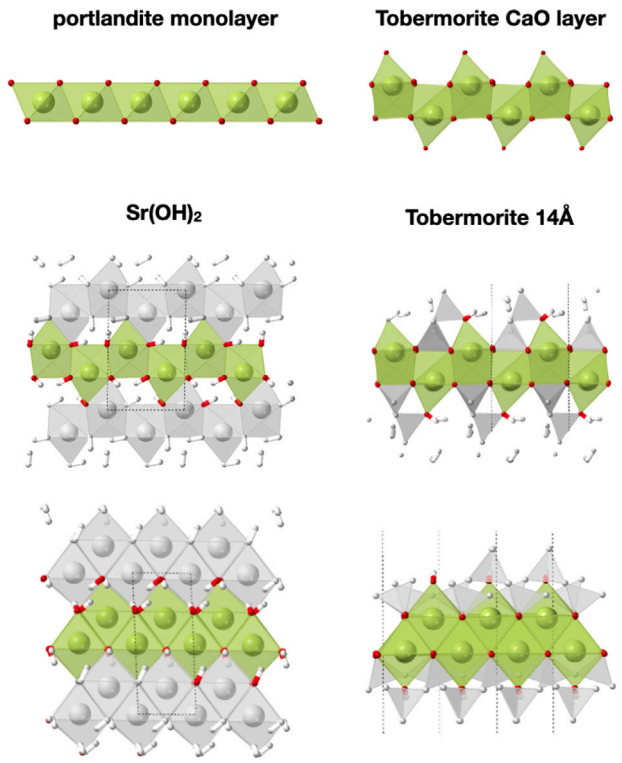

Fig. 2. The structures on top represent the portlandite monolayer and tobermorite Ca-O layer isolated from the crystals. The bottom ones represent two views of the crystalline structure of $Sr(OH)_2$ and tobermorite 14 Å. Only the coordination polyhedra of a Ca-O layer are colored for a better comparison.

2. Methods

DFT calculations were carried out using the Vienna *ab-initio* simulation package (VASP) [40–43] using the projector augmented wave method [44,45] and the GGA-optPBE [46,47] functional. This functional has been proved to represent correctly the van der Waals forces relevant for the description of portlandite and water-containing systems, for weakly interacting molecules [46] and bulk systems [47]. All the calculations were done with a Γ centered k-point mesh with a spacing of 0.025Å^{-1} in the reciprocal space. For the computation of the forces in the VC-NEB calculations, a plane wave energy cutoff of 450 eV was used, and the self consistent cycles were converged to 10^{-4} eV. On the other hand, for the structural relaxations more demanding calculations were performed with a plane wave energy cutoff of 550 eV and a convergence criterion for the self-consistent cycles of 10^{-6} eV. In these calculations, the ions were relaxed until the forces were lower than 0.01 eV/Å.

VC-NEB [48,49] calculations were performed using its implementation on the USPEX code [50–52]. A variable number of images (created by the interpolation of the atomic coordinates and cell vectors) were used between the initial and final structures of the transformation path, setting the average path length between consecutive images λ to 1.0. A new image was created each time the path length between two adjacent images was bigger than 1.5λ and removed when that distance was less than 0.5λ. The spring constant was set between 3–6 eV/Å and the steepest descend method was used for energy minimization with a step size of 0.1. The paths were minimized until the root mean square force of every image was less than 0.04 eV/Å.

The molecular dynamic simulations of both targeted molecular dynamics (TMD) and umbrella sampling (US) were done using the LAMMPS code [53] and the ReaxFF force field [54–56] with the Ca/Si/O/H set of parameters from ref. [56,57]. The velocity Verlet algorithm was used for the integration of the equations of motion with a time step of 0.1 fs. TMD calculations were performed in the NVT ensemble at 500 K to facilitate the condensation reactions, with a Nosé–Hoover thermostat with the temperature damping parameter set to 10 fs. US simulations were performed in the NPT ensemble at 300 K and 1 atm, with a Nosé–Hoover thermostat and barostat set with temperature and pressure damping parameters of 10 fs and 1000 fs respectively.

As the initial configuration of the TMD calculation, a portlandite monolayer (with periodic boundary conditions) was placed in a simulation box, with silicate dimmers at 3.3 Å above and below it. The pulling coordinate ρ was defined as the root mean square distance of the silicon atoms to the targeted position, which was set as the position of the dimers in a tobermorite monolayer. The silicon atoms were pulled over and restrained to the collective coordinate ρ, while the rest of the atoms in the system remained unrestrained. Two sets of simulations were done: a small system with a portlandite layer of 4 formula units surrounded by 2 silicate dimers, and a system four times larger. In the small cell calculation 100 trajectories were performed pulling the system from $\rho = 3.3$ Å to $\rho = 0.1$ Å at a constant pulling speed of $v_\rho = 0.083$ m/s. In the large cell calculation 50 trajectories were performed with a pulling rate of $v_\rho = 2$ m/s to sample the system from $\rho = 2.0$ Å to $\rho = 4.0$ Å, and a pulling rate of $v_\rho = 0.1$ m/s from $\rho = 2.0$ Å to $\rho = 0.1$ Å. The cell vector lengths of portlandite and tobermorite were slightly modified to avoid the mismatch between them. More detailed information about this process is available in the supplementary information.

Umbrella sampling calculations were carried out using the collective variables module implemented in LAMMPS [58]. The collective variable ρ was redefined as the projection onto the direction perpendicular to the layer so that it was not altered by the variable cell in the NPT ensemble. Along this reaction coordinate, 52 different stages were chosen to perform umbrella sampling simulations centered at those stages. Each simulation ran for 0.5 ns and the force constant of the spring attached to the reaction coordinate was set to 2.2 eV/Å. These parameters were chosen so that the whole reaction coordinate is properly sampled. For more information, the reader is referred to the supplementary information. The free energy ΔG was then reconstructed using the weighted histogram analysis method (WHAM) [59,60].

3. Results

3.1. Structural transformation in bulk portlandite

In our hypothesis presented in the introduction, we assume that portlandite precursor monolayers are formed in the mentioned dense liquid regions, and then suffer a topochemical structural transformation induced by the condensation of silicate dimers to form tobermorite monolayers. The final arrangement of the Ca-O layer in tobermorite is the same as in $Sr(OH)_2$ and therefore, we first investigate the feasibility of such structural transformation in the bulk $Ca(OH)_2$.

Besides portlandite [61], the stable phase at room conditions with symmetry $P\bar{3}m1$, various high pressure polymorphs of $Ca(OH)_2$ have been reported [62–65]. However, none of these phases has a similar layered structure to the one found in tobermorite. Such a layered structure can be found in the *Pnma* $Sr(OH)_2$. A $Ca(OH)_2$ polymorph with similarities to the $Sr(OH)_2$ phase has been reported before, but that structure has never been resolved [66]. Following the nomenclature used in the literature for other $Ca(OH)_2$ polymorphs, we will name the $Sr(OH)_2$-like structure "Phase V". The insights of this structural transformation would be particularly helpful to understand the C-S-H formation mechanism that we aim to study.

The structure of portlandite, Phase V and the other polymorphs were relaxed using DFT at different pressures. As expected, portlandite is the most stable structure at low pressures (see Fig. S1). Phase V is a metastable polymorph, with an energy difference with respect

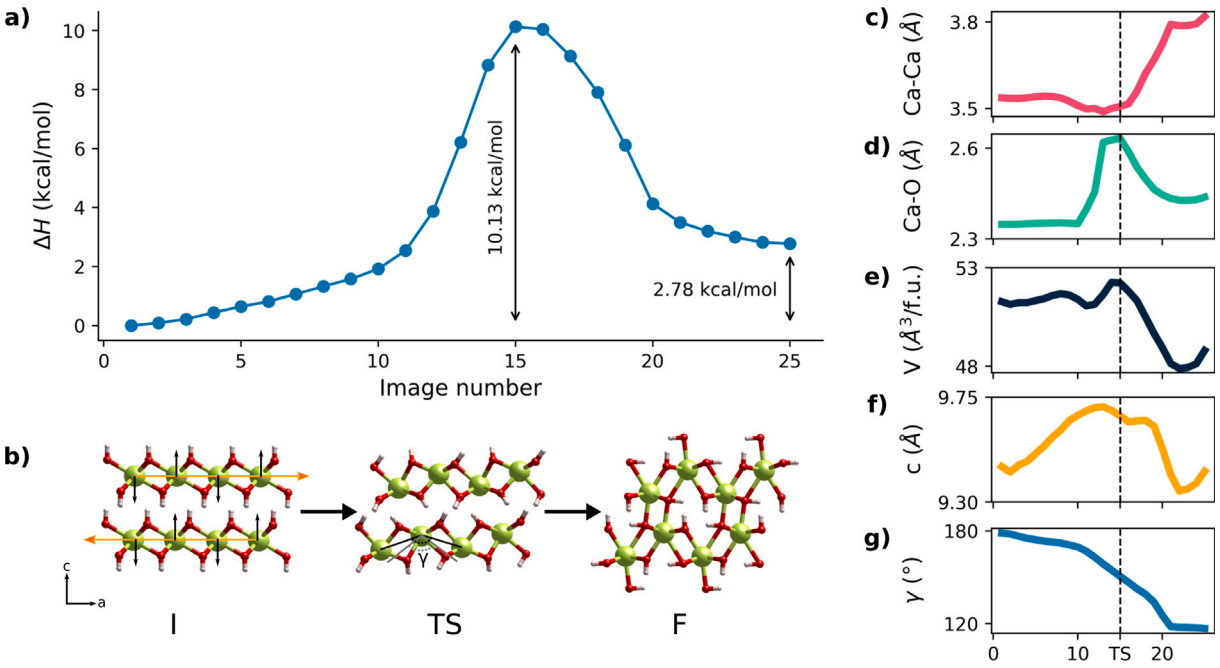

Fig. 3. Transformation path from portlandite to Phase V. (a) Enthalpy difference along with the structural transformation for each image used in the VC-NEB method. (b) Graphical representation of the different stages along with the structural transformation. The calcium, oxygen and hydrogen atoms are illustrated with green, red and pink spheres respectively. [(c)–(g)] Respectively, the evolution of the Ca-Ca intralayer distance, Ca-O mean distance, volume, c cell vector and the folding angle γ between three adjacent Ca atoms in the interlayer transformation path.

to portlandite of 2.78 kcal/mol at 0 GPa, a small value compared to other reported polymorphs at normal pressure. Therefore, the structural transformation from bulk portlandite to Phase V cannot be discarded. The atomic structure of the relaxed Phase V can be found in table S1.

The structural transformation between portlandite and Phase V was studied using the variable cell nudge elastic band (VC-NEB) method. In this method, intermediate images (structures) along the reaction path are created by interpolation of the atomic coordinates. The created images are then optimized simultaneously to find the optimal transformation path. We identified two different paths for the transformation: an interlayer and an intralayer path (see Fig. S2). The intralayer transformation is formed with several portlandite layers, that is, the direction of the layers at the beginning and at the end of the transformation are perpendicular. On the contrary, the interlayer transformation can occur in a single portlandite monolayer, as the orientation of the layers are maintained during the transformation. This makes this transformation path compatible with the nucleation model presented in the introduction. Thus, the interlayer transformation is the one investigated in detail.

The energy difference during the transformation path is plotted in Fig. 3(a) showing an energy barrier of 10.13 kcal/mol. This energy barrier is very similar to other energy barriers calculated for different bulk phase transitions as in bulk thorium monocarbide (ThC) or bulk GaN [49,67]. The computed transformation path shows a direct transformation with no local minimum in between. The low energy barrier and the fact that this transition can occur in a portlandite monolayer are promising factors for the study of the proposed mechanism for C-S-H formation. During the transition, the γ angle between three adjacent Ca atoms in the portlandite layer folds gradually to a 120° zig-zag layer Fig. 3(g). This folding is accompanied by a slight shift between layers and the readjustment of the H atoms to form the structure of Phase V. Several structural parameters were examined to understand the origin of the energy barrier. The evolution of the mean distance between the bonded Ca-O atoms is the parameter that better correlates with the energy [Fig. 3(d)]. As the Ca-O distance increases, the energy increases up to the transition state. Then, the Ca-O distance decreases to the final value, accompanied by an increase of the Ca-Ca mean distance and the unit cell volume.

Given that calcium and magnesium are isoelectronic, portlandite and brucite [$Mg(OH)_2$] share the same crystal structure. Hence, the possible stability of Phase V for $Mg(OH)_2$ is also checked. The structure is broken during the energy minimization process, which indicates that the phase is not even metastable. In fact, 7 fold Mg coordination has not been reported up to the authors knowledge. The impossibility of $Mg(OH)_2$ to adopt the crystalline arrangement of Phase V polymorph could be the reason why the M-S-H gels have a completely different structure from the tobermorite-like C-S-H gel [68].

3.2. Silicate reaction at portlandite surface

Once we have confirmed that the portlandite to Phase V transformation is feasible, we proceed to investigate the condensation reactions between a silicate dimer and a hydroxyl group from portlandite. According to the proposed mechanism, the formation of enough Si-O-Ca bonds will trigger the transformation from the flat portlandite monolayer into the zig-zag layer found in both tobermorite and Phase V.

The energy barrier of the condensation reaction was studied using nudged elastic band (NEB), taking 47 images between the initial (I) and final (F) stages of the transition [see Fig. 4(b)]. The initial stage consists of a portlandite monolayer and a silicate dimer placed at 5 Å from the surface. In the final stage, the silicate dimer is bonded to the portlandite layer with a Si-O-Ca bond, and a water molecule has been released. The conformations at the initial and final stages were minimized with DFT, and the intermediate images were created by interpolation of the atomic coordinates. Only one constraint was imposed based on our experience: as the covalent Si-O bond is generally stronger than the ionic Ca-O bond, the released water was formed by an oxygen atom belonging to the portlandite layer. This assumption was confirmed a posteriori in the MD simulations from Section 3.3, where we verified that in 99 % of the reactions water molecules were formed by oxygen atoms from portlandite.

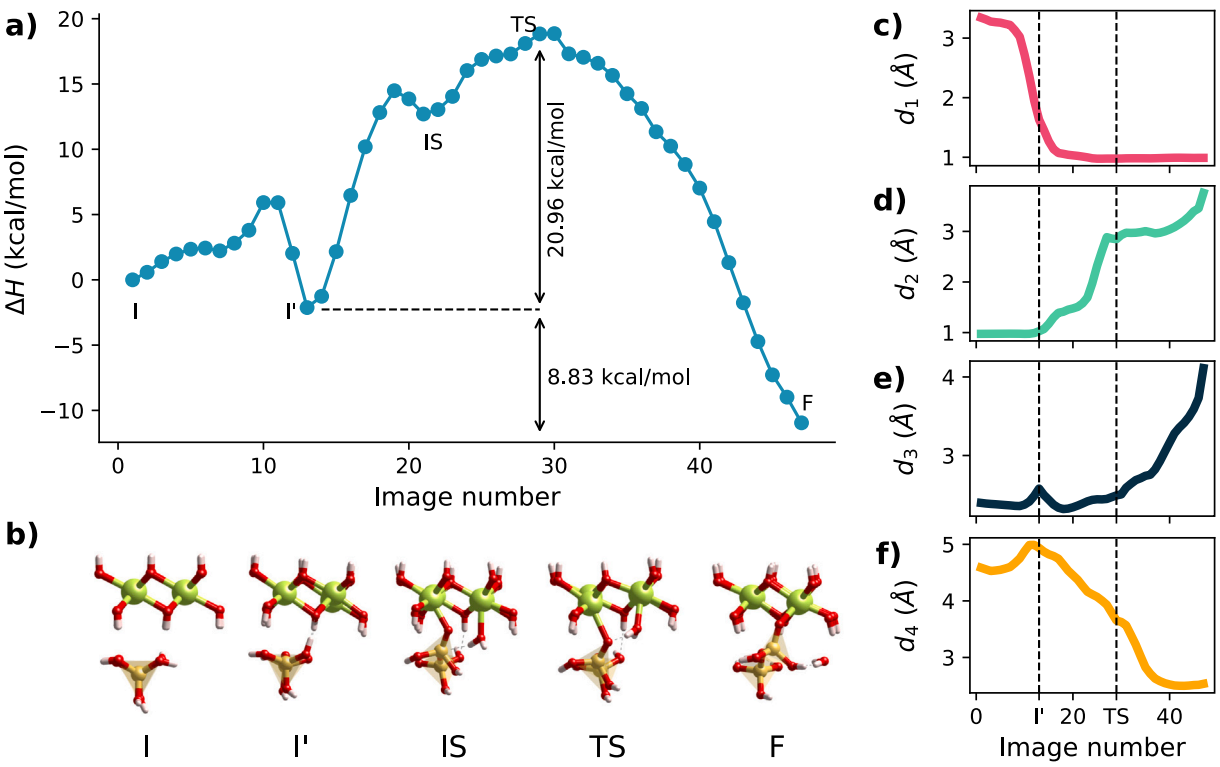

Fig. 4. Reaction path of the condensation of water in a Portlandite monolayer. (a) Enthalpy difference along the reaction path for each image used in the NEB method. (b) Graphical representation of the different stages along the condensation reaction. The calcium, silicon, oxygen and hydrogen atoms are illustrated with green, orange, red and pink spheres respectively. [(c)–(f)] d_1 represents the distance between the hydrogen atom in the silanol group and the oxygen atoms in the layer, d_2 the distance between the oxygen and hydrogen atoms of the silanol group, d_3 the distance between the oxygen in the layer and the calcium atom and d_4 the distance between the oxygen atom in the silanol group and the calcium atom. All these distances are plotted along the reaction path.

The minimized transition path presents different stages. In figure Fig. 4(a) we show the energy profile, together with bond distances of interest to characterize the reaction in Fig. 4(c–f). First, there is a reorientation of the silanol and hydroxyl groups involved in the condensation reaction, forming a hydrogen bond in which the silanol is the donor and portlandite the acceptor [sharp decrease of d_1 in Fig. 4(c)]. The reorientation energy barrier is 5.92 kcal/mol, and the resulting conformation I′ is more favorable than our initial guess I ($\Delta H = -2.13$ kcal/mol). From that stable conformation I′, there is a proton transfer reaction from the silanol to the hydroxyl group to form a water molecule in IS [increase of d_2 in Fig. 4(d)], with an associated activation energy of 16.61 kcal/mol. In the transition state (TS) the silicate and the water molecule are bonded to adjacent Ca atoms from portlandite. Finally, the water molecule is released [increase of d_3 in Fig. 4(e)] and the silicate oxygen is bonded to the layer [decrease of d_4 in Fig. 4(g)], completing the transition. The energy barrier from stage I′ to the TS is 20.96 kcal/mol and the enthalpy gain from stage I′ to the final stage is 8.83 kcal/mol. It is important to notice that the condensation reaction does not alter the portlandite conformation. Further reactions are needed to trigger the transformation, as we will see in the following subsection. The energy barrier is twice as high as that of the bulk portlandite transformation, and hence, the condensation reaction is likely the limiting process.

3.3. C-S-H monolayer formation

Now that the condensation reaction of silicates with portlandite is understood, the whole transformation from a portlandite to a tobermorite-like monolayer can be studied. To sample this transformation with molecular dynamics, the simulated time should be comparable to the transformation rate. Since such long simulations are computationally inaccessible, we have used two enhanced sampling techniques: targeted molecular dynamics (TMD) and umbrella sampling (US). First, TMD was used to obtain a reference transformation path, and then US was used for a good statistical sampling over that path. Although in typical cement conditions the portlandite monolayer would be in solution, for simplicity the simulations were done in vacuum.

TMD uses a time-dependent geometrical constraint to pull the system from the initial configuration towards the target structure [69,70]. It allows sampling the conformational space around a collective variable (a generic reaction coordinate) during the process [71,71,72]. In the TMD calculation, a portlandite monolayer (with periodic boundary conditions) was placed in a simulation box, with silicate dimmers at 3.3 Å above and below it. Longer chains with bridging silicates were not considered since those bridging sites would not participate in the transformation. The pulling coordinate ρ was defined as the root mean square distance of the silicon atoms to the targeted position, which was set as the position of the dimers in a tobermorite monolayer. The silicon atoms were dragged over and restrained to the collective coordinate ρ. The rest of the atoms in the system remained unrestrained. The simulations were done at 500 K to accelerate the condensation reaction rate.

In Fig. 5(a) we show the internal energy as a function of the collective variable ρ for all the trajectories. The color of each point indicates the percentage of condensation reactions that took place with respect to a fully reacted system. From $\rho = 3.3$ Å to $\rho = 1.65$ Å no reactions were observed as the silicate dimmers approach the $Ca(OH)_2$ monolayer. Then, condensation reactions start following the mechanism described in Section 3.2. The distance ρ at which the first condensation reactions take place is relatively homogeneous across simulations. Subsequent reactions take place at a different rate, and two sets of trajectories can be identified: those with a completed transformation and those with an uncompleted transformation. The completion of the transformation strongly depends on the percentage of chemical reactions the system

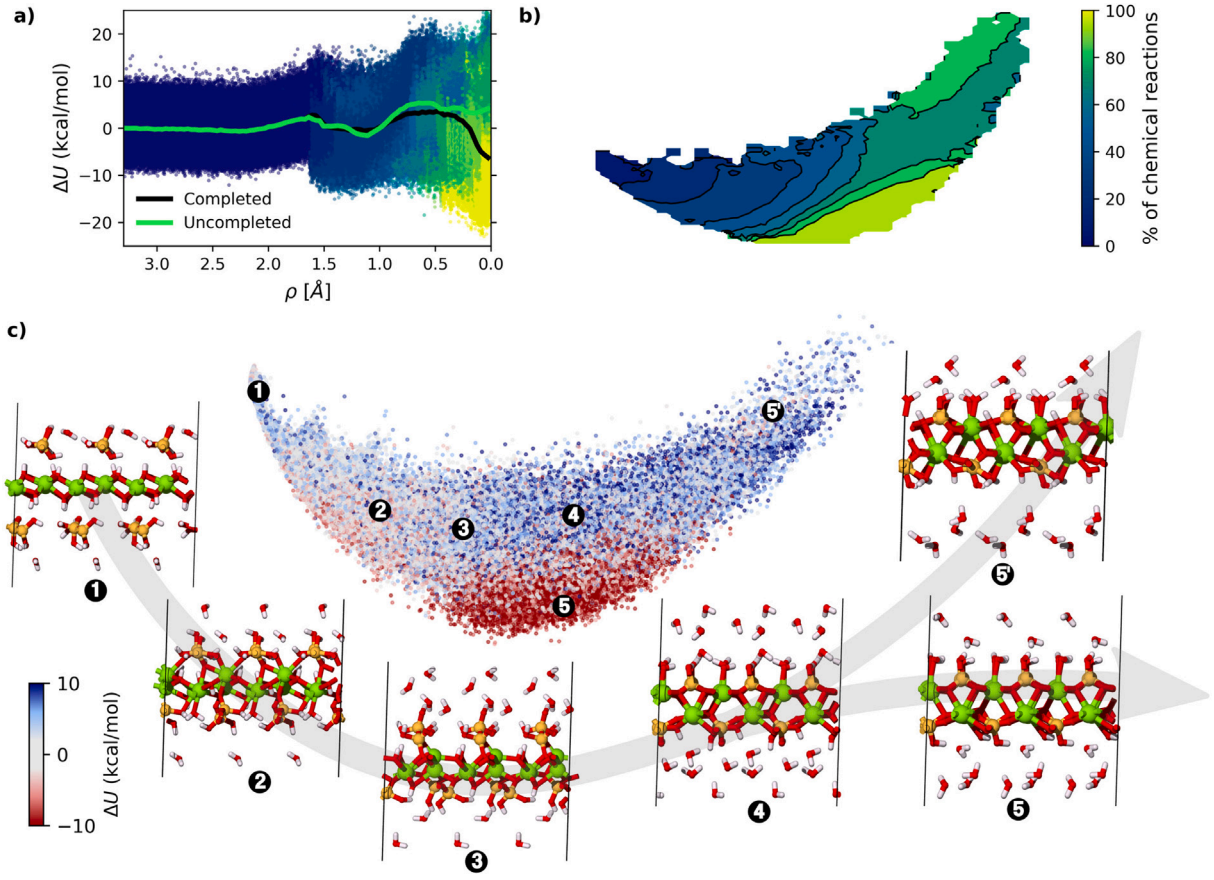

Fig. 5. Topochemically induced transformation from a portlandite monolayer to a C-S-H layer computed with TMD. (a) Internal energy difference of the 100 trajectories along the pulling coordinate. The dots represent different snapshots of the trajectories and the solid lines represent the mean value of the internal energy for the completed (black) and uncompleted (green) trajectories. The color scheme represents the percentage of condensation reactions needed for the complete process. (b) The average percentage of the condensation reactions along with the first two components of the KPCA. The distance in the plot represents the structural distance calculated with SOAP. The portlandite monolayer is located in the areas where 0 % of the reactions have occurred and the C-S-H monolayer is located in the areas where 100 % of the reactions have occurred. (c) Internal energy difference of 100.000 snapshots of the trajectories along with the two first components of the KPCA. Each dot represents a snapshot and the distance between dots represents the structural distance calculated with SOAP. The color scheme represents the internal energy difference of each snapshot.

has gone through. When some hydroxyl groups in the portlandite layer remain unreacted, the structure evolves to a final defective tobermorite-like monolayer with interstitial hydrogen atoms on it. These defects have important energetic consequences. In Fig. 5(a) the solid lines represent the average internal energy of all the completed and uncompleted trajectories as a function of ρ. The black color was used for fully reacted systems, and green for uncompleted systems. Up to $\rho = 1.65$ Å, before the chemical reactions start, both sets are equivalent. Then, for $\rho < 1.65$ Å, when the reactions start, the mean internal energies start to slightly deviate. However, it is not until $\rho < 0.25$ Å that there is a significant difference between both sets. The completed trajectories experience a final energy decrease of −6.24 kcal/mol, making them more stable. The uncompleted trajectories end up with a 4.19 kcal/mol increase in energy. It is important to notice that the drop in energy in the completed trajectories only happens when the percentage of condensation reactions is close to 100 %. Hence, the system only stabilizes when the process is totally completed. Therefore, it can be stated that the chemical reactions that drive the transformation are fully accessible from the internal energy perspective.

To elucidate whether the two sets of trajectories are due to divergent paths or the existence of two final (meta)stable structures, we did a structural distance analysis. We used the smooth overlap of atomic positions descriptor (SOAP) [73,74] to compute structural distances and the kernel principal component analysis (KPCA) to reduce the dimensionality of the computed distance matrix [75], plotting it in 2D. In the resulting plots [Fig. 5(b) and Fig. 5(c)] the distance between points represent their structural similarity. In addition, the color scale in Fig. 5(b) indicates the percentage of occurred condensation reactions, while the color scheme in Fig. 5(c) represents the internal energy difference with respect to the starting configuration. The structural distance plotted in Fig. 5(b) clearly shows that there is mostly one single path until 60% of reactions occur. However, at the end of the simulations, two limiting regions can be found concerning the condensation reaction percentage. The upper right area corresponds to uncompleted trajectories, while the bottom area in the plot corresponds to completed trajectories where all the reactions have occurred. Since we have already stated that the transformation evolves along with the percentage of chemical reactions, it is clear now that the completed and uncompleted trajectories end up in structurally slightly different regions.

This is illustrated in Fig. 5(c), where the internal energy difference and snapshots of some obtained structures during the transformation are shown. The snapshots represent the evolution towards the complete (number 5) and incomplete (number 5') transformation. It can be seen in snapshots 1–3 that for the first 30% of the reactions, the layer is not bent at all. Until here, both the complete and incomplete trajectories follow the same trend. It is not until 50%–60% of the reactions have occurred (snapshot 4) that the layer starts to take the zig-zagged form of tobermorite. Finally, both the complete and incomplete trajectories (snapshots 5 and 5′ respectively) reach the zig-zag structure of tobermorite. However, Some hydroxyl groups attached to the layer are still found in the final state of the uncompleted trajectories, which is unfavorable. In terms of energy, it can be observed again that the final

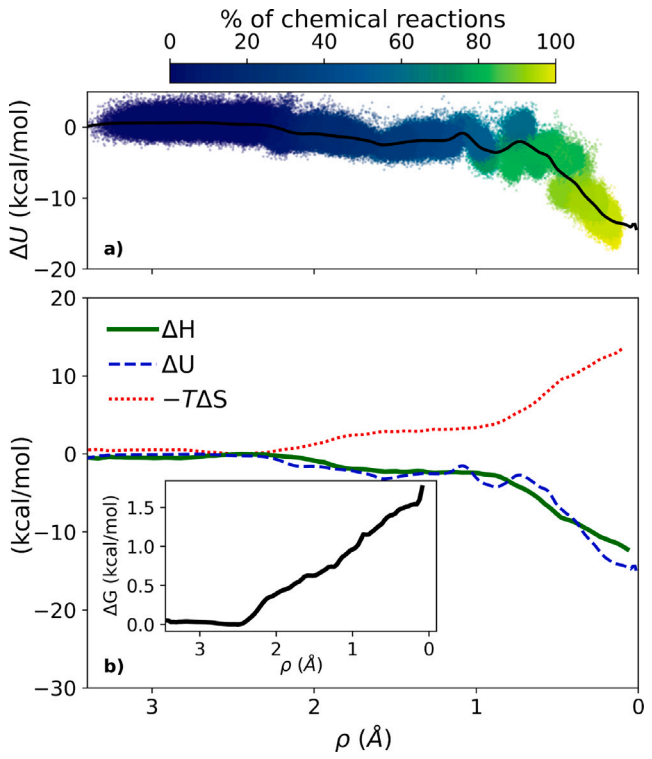

Fig. 6. (a) Internal energy difference of the umbrella sampling trajectories along the pulling coordinate. The color scheme represents the percentage of condensation reactions needed for the complete process. (b) The thermodynamical properties of the process along the pulling coordinate.

state of a completed trajectory has much lower energy than the final state from an uncompleted trajectory.

To compute the free energy of the transformation, we performed umbrella sampling (US) of a complete trajectory obtained from TMD. In US the trajectory is divided into windows along the reaction coordinate, and then independent simulations are done for each window, restraining the system by a biased potential [76,77]. To improve the sampling conditions, the US calculations were done in a unit cell four times larger than the previous TMD simulations, and the NPT ensemble was used to relax also the layer area. In addition, the simulation temperature could be lowered to 300 K, as the condensation reactions are already reproduced in the initial trajectory.

Fig. 6(a) shows that the internal energy difference between the portlandite layer surrounded by silicate dimers (ρ = 3.3 Å) and the tobermorite layer (ρ = 0.0 Å) is 15 kcal/mol. This value is larger than that from TMD due to the additional volumetric relaxation. As a matter of fact, the area of the layer decreases by 12.6 % as it reacts. The compression is mostly found in the direction perpendicular to the silicate dimers, which exhibits an 11.1 % decrease. The layer starts to get compressed after around 20 % of the chemical reactions have occurred and it follows this trend almost constantly until the end of the transition.

In addition to the internal energy, the sampling made with US allowed us to compute the main thermodynamical properties of the process, i.e., the enthalpy, the free energy and the entropy. As seen in the previous section, the internal energy drop starts when most (more than 80%) of the chemical reactions have taken place. As expected from an NPT simulation, the enthalpy and the internal energy are mostly the same. However, the reaction free energy increases monotonically for the entire transition due to the entropic contribution ($T\Delta S$), see Fig. 6(b). This monotonical increase in free energy makes the transformation not spontaneous from a thermodynamical point of view. The free energy starts to grow just when the first condensation reactions take place, and no energy barrier was found. The reason behind the increase in ΔG is a decrease of the system entropy, $\Delta G = \Delta H - T\Delta S$. We suggest that the condensation reactions impose a decrease of the translational and vibrational degrees of freedom, decreasing the entropy. This scenario should be usual for any nucleation and growth process, yet in the present case, the gain on enthalpy cannot compensate for such an entropy diminution.

4. Discussion

According to our simulations, the free energy of the transformation from a portlandite monolayer to a tobermorite-like monolayer is ΔG_r^0 = 1.5 kcal/mol. In the present case, the internal energy and the enthalpy are both negative and with a very similar magnitude (−14.95 and −12.21 kcal/mol), yet there is a decrease in the term $T\Delta S_r^0$ of 13.5 kcal/mol associated to the reduction of the translational and vibrational degrees of freedom during the C-S-H monolayer formation.

We can compare the studied reaction with the expected results from thermodynamic data. The comparison can only be qualitative due to the different thermodynamic conditions. In the proposed transformation path the reactants are solid portlandite and fully protonated silicate dimers. From our calculations we obtain:

$$2Ca(OH)_{2(s)} + Si_2O(OH)_6 \longrightarrow Ca_2Si_2O_5(OH)_2 + 4H^+H_2O \qquad \Delta G_1^0 = 3 \text{ kcal/mol.}$$

The standard free energy of reactions for portlandite [78,79] and the silicate dimmers [80,81] are:

$$Ca^{2+} + 2H_2O \longrightarrow Ca(OH)_{2(s)} + 2H^+ \qquad \Delta G_2^0 = 31.2 \text{ kcal/mol}$$

and

$$2Si(OH)_4 \longrightarrow Si_2O(OH)_6 + H_2O \qquad \Delta G_3^0 = -3.5 \text{ kcal/mol.}$$

Therefore, constructing a Hess cycle the ΔG_f for the reaction from the monomeric species in solution to form the C-S-H monolayer with the intermediate step of portlandite formation and silica polymerization is:

$$2Ca^{2+} + 2Si(OH)_4 \longrightarrow Ca_2Si_2O_5(OH)_2 + H_2O + 4H^+ \qquad \Delta G_f^0 = 61.9 \text{ kcal/mol.}$$

The result ΔG_r = 61.9 kcal/mol is considerably higher, ≈ 20 kcal/mol, than the value calculated by Haas and Nonat for the same reaction to form a C-S-H with the same composition (C-S-H-β, ΔG_r^0 = 40.4 kcal/mol) [82]. The discrepancy can be ascribed to computational aspects or to the model. Methodological aspects like a correct trajectory sampling and the accuracy of the ReaxFF energies have been evaluated, and do not represent a relevant source of error (results in Fig. S7). However, the thermodynamic conditions of the simulations might account for the difference. The proposed reaction takes place on a portlandite monolayer, far from the standard thermodynamic conditions that assume infinite crystals. In our system, we can expect that the contribution of the surface free energy to the total free energy will be important. Furthermore, the composition of a monolayer will differ from a bulky crystal of C-S-H where layers are stacked by interlaminar Ca atoms not present in our monolayer. Moreover, our simulations are done in the gas phase, i.e., water as a solvent is not included.

The aim of this work was to test a hypothetical mechanism for the C-S-H formation at the nanoscale. In this regard, we proved that the mechanism is feasible and that portlandite can react with silicate

species in solution via condensation reactions to form C-S-H monolayers. The internal energy and enthalpy of the formation reactions indicate that it is a favorable transformation. Nevertheless, the exact thermodynamic conditions must be carefully evaluated to understand if this could be a feasible step in C-S-H formation, at least under certain conditions. The results suggest that the reaction free energy of the proposed scenario for the formation of C-S-H is principally governed by the formation of portlandite nanoclusters, since the transformation from a portlandite monolayer to a C-S-H monolayer does not contribute substantially to the overall free energy of formation. As a matter of fact, at high pH both the formation of portlandite and C-S-H become negative, $\Delta G_f^0 = -214.4$ kcal/mol [83] and $\Delta G_f^0 = -855.54$ kcal/mol [79, 84] respectively, while the silicate dimerization free energy becomes positive [80], supporting the key role of portlandite formation in the process. Finally, we must also take into account that Ca and silicic acid form complexes in solution [85,86] which could hinder the formation of nanoportlandite, leading to a different mechanism based on the aggregation of complexes.

5. Conclusions

The nucleation of the C-S-H gel plays a key role in the early stages of cement hydration, influencing the hydration rate and the cement microstructure development. Although various experimental and theoretical works have helped to understand some aspects of C-S-H nucleation, the main atomic mechanism of C-S-H crystallization is still unknown. In this work, we have proposed a model for C-S-H crystallization based on a chemically induced transformation from a portlandite monolayer to a C-S-H monolayer.

First, the different steps of the process have been studied independently by DFT. The hypothetical transformation from bulk portlandite to bulk Phase V polymorph (with a tobermorite-like arrangement of the Ca-O structure) is favorable and has a low energy barrier (10.13 kcal/mol). The condensation reaction of a silicate dimer with a portlandite monolayer is also favorable (−8.83 kcal/mol), but has a larger energy barrier of 20.96 kcal/mol. When the complete process is simulated using molecular dynamics, we observe that enough condensation reactions are indeed able to trigger the transformation from portlandite to C-S-H. The internal energy is favorable (−15 kcal/mol) although the free energy obtained from umbrella sampling is positive (1.5 kcal/mol). From a qualitative point of view, this free energy value is in a reasonable range that makes the studied process a potential C-S-H formation pathway. The proposed formation pathway does not exclude other possible formation mechanisms, and may exist alongside others.

Overall, this work not only proposes a plausible model for the formation of the C-S-H gel, but also establishes a series of computational methods that can be used in the future to study other nucleation conditions. As a matter of fact, future work in more realistic thermodynamic conditions will be necessary to determine if the proposed crystallization pathway is feasible and under what conditions. In this regard, the portlandite monolayer nucleation conditions are particularly interesting.

CRediT authorship contribution statement

Xabier M. Aretxabaleta: Methodology, Validation, Formal analysis, Investigation, Writing – original draft, Writing – review & editing, Visualization. **Jon López-Zorrilla:** Investigation, Writing – review & editing. **Christophe Labbez:** Formal analysis, Investigation, Writing – review & editing. **Iñigo Etxebarria:** Investigation, Writing – review & editing. **Hegoi Manzano:** Conceptualization, Investigation, Writing – original draft, Writing – review & editing, Supervision, Project administration, Visualization.

Declaration of competing interest

The authors declare that they have no known competing financial interests or personal relationships that could have appeared to influence the work reported in this paper.

Data availability

Data will be made available on request.

Acknowledgments

This work was supported by the “Departamento de Educación, Política Lingüística y Cultura del Gobierno Vasco” (IT1458-22) and the “Ministerio de Ciencia e Innovación" (PID2019-106644GB-I00). The authors thank for technical and human support provided by SGIker (UPV/EHU/ ERDF, EU). X.M.A. acknowledges the financial support from the University of the Basque Country, UPV/EHU (PIF17/118), and J.L.-Z. the financial support from the Basque Country Government (PRE_2019_1_0025).

Appendix A. Supplementary data

Supplementary material related to this article can be found online at https://doi.org/10.1016/j.cemconres.2022.106965.

References

[1] P.K. Mehta, H. Meryman, Tools for reducing carbon emissions due to cement consumption, Structure 1 (1) (2009) 11–15.
[2] American geological survey, 2020, Cement annual publication 2020, https://pubs.usgs.gov/periodicals/mcs2021/mcs2021-cement.pdf.
[3] C. Li, X.Z. Gong, S.P. Cui, Z.H. Wang, Y. Zheng, B.C. Chi, CO2 emissions due to cement manufacture, in: Mater. Sci. Forum, 685, Trans Tech Publ, 2011, pp. 181–187.
[4] S. Merlino, E. Bonaccorsi, T. Armbruster, The real structure of tobermorite 11A: Normal and anomalous forms, OD character and polytypic modifications, Eur. J. Mineral. 13 (3) (2001) 577–590.
[5] J. Bernal, J. Jeffery, H. Taylor, Crystallographic research on the hydration of Portland cement. A first report on investigations in progress, Mag. Concr. Res. 4 (11) (1952) 49–54.
[6] H. Stade, D. Müller, On the coordination of al in ill-crystallized CSH phases formed by hydration of tricalcium silicate and by precipitation reactions at ambient temperature, Cem. Concr. Res. 17 (4) (1987) 553–561.
[7] L.D. Glasser, E. Lachowski, K. Mohan, H. Taylor, A multi-method study of C3S hydration, Cem. Concr. Res. 8 (6) (1978) 733–739.
[8] K. Scrivener, A. Ouzia, P. Juilland, A. Kunhi Mohamed, Advances in understanding cement hydration mechanisms, Cem. Concr. Res. 124 (2019) 105823, http://dx.doi.org/10.1016/j.cemconres.2019.105823, URL https://www.sciencedirect.com/science/article/pii/S0008884619308051.
[9] S. Garrault-Gauffinet, A. Nonat, Experimental investigation of calcium silicate hydrate (CSH) nucleation, J. Cryst. Growth 200 (3–4) (1999) 565–574.
[10] S. Garrault, E. Finot, E. Lesniewska, A. Nonat, Study of CSH growth on C 3 S surface during its early hydration, Mater. Struct. 38 (4) (2005) 435–442.
[11] R. Alizadeh, L. Raki, J.M. Makar, J.J. Beaudoin, I. Moudrakovski, Hydration of tricalcium silicate in the presence of synthetic calcium–silicate–hydrate, J. Mater. Chem. 19 (42) (2009) 7937–7946.
[12] E. John, T. Matschei, D. Stephan, Nucleation seeding with calcium silicate hydrate–A review, Cem. Concr. Res. 113 (2018) 74–85.
[13] C. Nalet, A. Nonat, Effects of functionality and stereochemistry of small organic molecules on the hydration of tricalcium silicate, Cem. Concr. Res. 87 (2016) 97–104.
[14] P. Juilland, E. Gallucci, Hindered calcium hydroxide nucleation and growth as mechanism responsible for tricalcium silicate retardation in presence of sucrose, Special Publ. 329 (2018) 143–154.
[15] N. Krautwurst, L. Nicoleau, M. Dietzsch, I. Lieberwirth, C. Labbez, A. Fernandez-Martinez, A.E. Van Driessche, B. Barton, S. Leukel, W. Tremel, Two-step nucleation process of calcium silicate hydrate, the nanobrick of cement, Chem. Mater. 30 (9) (2018) 2895–2904.
[16] J. Plank, M. Schönlein, V. Kanchanason, Study on the early crystallization of calcium silicate hydrate (CSH) in the presence of polycarboxylate superplasticizers, J. Organomet. Chem. 869 (2018) 227–232.
[17] E. Masoero, Mesoscale mechanisms of cement hydration: BNG model and particle simulations, in: Handbook of Materials Modeling: Applications: Current and Emerging Materials, 2018.

[18] E. Masoero, J.J. Thomas, H.M. Jennings, A reaction zone hypothesis for the effects of particle size and water-to-cement ratio on the early hydration kinetics of C3S, J. Am. Ceram. Soc. 97 (3) (2014) 967–975.

[19] J.J. Thomas, A new approach to modeling the nucleation and growth kinetics of tricalcium silicate hydration, J. Am. Ceram. Soc. 90 (10) (2007) 3282–3288.

[20] A. Kumar, S. Bishnoi, K.L. Scrivener, Modelling early age hydration kinetics of alite, Cem. Concr. Res. 42 (7) (2012) 903–918.

[21] R. Gonzalez-Teresa, J.S. Dolado, A. Ayuela, J.-C. Gimel, Nanoscale texture development of CSH gel: A computational model for nucleation and growth, Appl. Phys. Lett. 103 (23) (2013) 234105.

[22] I. Shvab, L. Brochard, H. Manzano, E. Masoero, Precipitation mechanisms of mesoporous nanoparticle aggregates: Off-lattice, coarse-grained, kinetic simulations, Cryst. Growth Des. 17 (3) (2017) 1316–1327.

[23] E. Del Gado, K. Ioannidou, E. Masoero, A. Baronnet, R.-M. Pellenq, F.-J. Ulm, S. Yip, A soft matter in construction–statistical physics approach to formation and mechanics of C–S–H gels in cement, Eur. Phys. J. Spec. Top. 223 (11) (2014) 2285–2295.

[24] K. Ioannidou, K.J. Krakowiak, M. Bauchy, C.G. Hoover, E. Masoero, S. Yip, F.-J. Ulm, P. Levitz, R.J.-M. Pellenq, E. Del Gado, Mesoscale texture of cement hydrates, Proc. Natl. Acad. Sci. 113 (8) (2016) 2029–2034.

[25] L. Nguyen-Tuan, M.A. Etzold, C. Rößler, H.-M. Ludwig, Growth and porosity of C-S-H phases using the sheet growth model, Cem. Concr. Res. 129 (2020) 105960, http://dx.doi.org/10.1016/j.cemconres.2019.105960, URL https://www.sciencedirect.com/science/article/pii/S0008884619306428.

[26] G.C. Sosso, J. Chen, S.J. Cox, M. Fitzner, P. Pedevilla, A. Zen, A. Michaelides, Crystal nucleation in liquids: Open questions and future challenges in molecular dynamics simulations, Chem. Rev. 116 (12) (2016) 7078–7116.

[27] H. Manzano, A. Ayuela, J. Dolado, On the formation of cementitious C–S–H nanoparticles, J. Comput.-Aided Mater. Des. 14 (1) (2007) 45–51.

[28] K. Yang, C.E. White, Modeling of aqueous species interaction energies prior to nucleation in cement-based gel systems, Cem. Concr. Res. 139 (2021) 106266.

[29] J.S. Dolado, M. Griebel, J. Hamaekers, A molecular dynamic study of cementitious calcium silicate hydrate (C–S–H) gels, J. Am. Ceram. Soc. 90 (12) (2007) 3938–3942.

[30] J.S. Dolado, M. Griebel, J. Hamaekers, F. Heber, The nano-branched structure of cementitious calcium–silicate–hydrate gel, J. Mater. Chem. 21 (12) (2011) 4445–4449.

[31] H. Manzano, J.S. Dolado, M. Griebel, J. Hamaekers, A molecular dynamics study of the aluminosilicate chains structure in Al-rich calcium silicate hydrated (C–S–H) gels, Phys. Status Solidi (A) 205 (6) (2008) 1324–1329.

[32] J. Bernal, The structures of cement hydration compounds, in: Proc. 3rd Int. Symp. Chem. Cem., London: Cement and Concrete Association, 1952, pp. 216–236.

[33] J. Bernal, J. Jeffery, H. Taylor, Crystallographic research on the hydration of portland cement. A first report on investigations in progress, Mag. Concr. Res. 4 (11) (1952) 49–54.

[34] X. Cong, R.J. Kirkpatrick, 29Si MAS NMR study of the structure of calcium silicate hydrate, Adv. Cem. Based Mater. 3 (3–4) (1996) 144–156.

[35] H. Taylor, J. Howison, Relationships between calcium silicates and clay minerals, Clay Miner. Bull. 3 (16) (1956) 98–111.

[36] A. Cuesta, J.D. Zea-Garcia, D. Londono-Zuluaga, G. Angeles, I. Santacruz, O. Vallcorba, M. Dapiaggi, S.G. Sanfélix, M.A. Aranda, Multiscale understanding of tricalcium silicate hydration reactions, Sci. Rep. 8 (1) (2018) 1–11.

[37] S. Grangeon, A. Fernandez-Martinez, A. Baronnet, N. Marty, A. Poulain, E. Elkaim, C. Roosz, S. Gaboreau, P. Henocq, F. Claret, Quantitative X-ray pair distribution function analysis of nanocrystalline calcium silicate hydrates: A contribution to the understanding of cement chemistry, J. Appl. Crystallogr. 50 (1) (2017) 14–21.

[38] Q. Zheng, J. Jiang, G. Xu, J. Yu, L. Tang, S. Li, New insights into the role of portlandite in the cement system: Elastic anisotropy, thermal stability, and structural compatibility with CSH, Cryst. Growth Des. 20 (4) (2020) 2477–2488.

[39] A. Kumar, B.J. Walder, A. Kunhi Mohamed, A. Hofstetter, B. Srinivasan, A.J. Rossini, K. Scrivener, L. Emsley, P. Bowen, The atomic-level structure of cementitious calcium silicate hydrate, J. Phys. Chem. C 121 (32) (2017) 17188–17196.

[40] G. Kresse, J. Hafner, Ab initio molecular dynamics for liquid metals, Phys. Rev. B 47 (1) (1993) 558.

[41] G. Kresse, J. Hafner, Ab initio molecular-dynamics simulation of the liquid-metal–amorphous-semiconductor transition in germanium, Phys. Rev. B 49 (20) (1994) 14251.

[42] G. Kresse, J. Furthmüller, Efficiency of ab-initio total energy calculations for metals and semiconductors using a plane-wave basis set, Comput. Mater. Sci. 6 (1) (1996) 15–50.

[43] G. Kresse, J. Furthmüller, Efficient iterative schemes for ab initio total-energy calculations using a plane-wave basis set, Phys. Rev. B 54 (16) (1996) 11169.

[44] P.E. Blöchl, Projector augmented-wave method, Phys. Rev. B 50 (24) (1994) 17953.

[45] G. Kresse, D. Joubert, From ultrasoft pseudopotentials to the projector augmented-wave method, Phys. Rev. B 59 (3) (1999) 1758.

[46] J. Klimeš, D.R. Bowler, A. Michaelides, Chemical accuracy for the van der Waals density functional, J. Phys.: Condens. Matter 22 (2) (2009) 022201.

[47] J. Klimeš, D.R. Bowler, A. Michaelides, Van der Waals density functionals applied to solids, Phys. Rev. B 83 (19) (2011) 195131.

[48] G. Henkelman, H. Jónsson, Improved tangent estimate in the nudged elastic band method for finding minimum energy paths and saddle points, J. Chem. Phys. 113 (22) (2000) 9978–9985.

[49] G.-R. Qian, X. Dong, X.-F. Zhou, Y. Tian, A.R. Oganov, H.-T. Wang, Variable cell nudged elastic band method for studying solid–solid structural phase transitions, Comput. Phys. Comm. 184 (9) (2013) 2111–2118, http://dx.doi.org/10.1016/j.cpc.2013.04.004, URL http://www.sciencedirect.com/science/article/pii/S0010465513001392.

[50] A.R. Oganov, C.W. Glass, Crystal structure prediction using ab initio evolutionary techniques: Principles and applications, J. Chem. Phys. 124 (24) (2006) 244704.

[51] A.R. Oganov, A.O. Lyakhov, M. Valle, How evolutionary crystal structure prediction works and why, Acc. Chem. Res. 44 (3) (2011) 227–237.

[52] A.O. Lyakhov, A.R. Oganov, H.T. Stokes, Q. Zhu, New developments in evolutionary structure prediction algorithm USPEX, Comput. Phys. Comm. 184 (4) (2013) 1172–1182.

[53] S. Plimpton, Fast parallel algorithms for short-range molecular dynamics, J. Comput. Phys. 117 (1) (1995) 1–19.

[54] A.C. Van Duin, S. Dasgupta, F. Lorant, W.A. Goddard, ReaxFF: A reactive force field for hydrocarbons, J. Phys. Chem. A 105 (41) (2001) 9396–9409.

[55] A.C. Van Duin, A. Strachan, S. Stewman, Q. Zhang, X. Xu, W.A. Goddard, Reaxffsio reactive force field for silicon and silicon oxide systems, J. Phys. Chem. A 107 (19) (2003) 3803–3811.

[56] H. Manzano, R.J. Pellenq, F.-J. Ulm, M.J. Buehler, A.C. van Duin, Hydration of calcium oxide surface predicted by reactive force field molecular dynamics, Langmuir 28 (9) (2012) 4187–4197.

[57] H. Manzano, S. Moeini, F. Marinelli, A.C. Van Duin, F.-J. Ulm, R.J.-M. Pellenq, Confined water dissociation in microporous defective silicates: Mechanism, dipole distribution, and impact on substrate properties, J. Am. Chem. Soc. 134 (4) (2012) 2208–2215.

[58] G. Fiorin, M.L. Klein, J. Hénin, Using collective variables to drive molecular dynamics simulations, Mol. Phys. 111 (22–23) (2013) 3345–3362.

[59] A. Grossfield, WHAM; the wighted histrogram analysis method, version 2.0.11, URL http://membrane.urmc.rochester.edu/wordpress/?page_id=126.

[60] M. Souaille, B. Roux, Extension to the weighted histogram analysis method: Combining umbrella sampling with free energy calculations, Comput. Phys. Comm. 135 (1) (2001) 40–57.

[61] T. Nagai, T. Ito, T. Hattori, T. Yamanaka, Compression mechanism and amorphization of portlandite, Ca (OH) 2: Structural refinement under pressure, Physics and Chemistry of Minerals 27 (7) (2000) 462–466.

[62] R. Dupuis, J.S. Dolado, M. Benoit, J. Surga, A. Ayuela, Quantum nuclear dynamics of protons within layered hydroxides at high pressure, Sci. Rep. 7 (1) (2017) 1–7.

[63] K. Leinenweber, D.E. Partin, U. Schuelke, M. O'Keeffe, R.B. Von Dreele, The structure of high pressure Ca (OD) 2II from powder neutron diffraction: Relationship to the ZrO2and EuI2Structures, J. Solid State Chem. 132 (2) (1997) 267–273.

[64] R. Iizuka, T. Yagi, K. Komatsu, H. Gotou, T. Tsuchiya, K. Kusaba, H. Kagi, Crystal structure of the high-pressure phase of calcium hydroxide, portlandite: In situ powder and single-crystal X-ray diffraction study, Am. Mineralogist 98 (8–9) (2013) 1421–1428.

[65] S. Shao, J. Bi, P. Gao, G. Liu, M. Zhou, J. Lv, Y. Xie, Y. Wang, Stability of Ca (OH) 2 at Earth's deep lower mantle conditions, Phys. Rev. B 104 (1) (2021) 014107.

[66] S. Ekbundit, K. Leinenweber, J. Yarger, J. Robinson, M. Verhelst-Voorhees, G. Wolf, New high-pressure phase and pressure-induced amorphization of Ca (OH) 2: Grain size effect, J. Solid State Chem. 126 (2) (1996) 300–307.

[67] R. Zhang, S. Zhang, Y. Guo, Z. Fu, D. Legut, T.C. Germann, S. Veprek, First-principles design of strong solids: Approaches and applications, Phys. Rep. 826 (2019) 1–49.

[68] E. Bernard, B. Lothenbach, C. Chlique, M. Wyrzykowski, A. Dauzeres, I. Pochard, C. Cau-Dit-Coumes, Characterization of magnesium silicate hydrate (MSH), Cem. Concr. Res. 116 (2019) 309–330.

[69] J. Schlitter, M. Engels, P. Krüger, Targeted molecular dynamics: A new approach for searching pathways of conformational transitions, J. Mol. Graph. 12 (2) (1994) 84–89, http://dx.doi.org/10.1016/0263-7855(94)80072-3, URL http://www.sciencedirect.com/science/article/pii/0263785594800723.

[70] J. Schlitter, W. Swegat, T. Mülders, Distance-type reaction coordinates for modelling activated processes, Mol. Model. Annu. 7 (6) (2001) 171–177.

[71] M. Post, S. Wolf, G. Stock, Principal component analysis of nonequilibrium molecular dynamics simulations, J. Chem. Phys. 150 (20) (2019) 204110.

[72] P. Ferrara, J. Apostolakis, A. Caflisch, Computer simulations of protein folding by targeted molecular dynamics, Proteins: Struct., Funct., and Bioinform. 39 (3) (2000) 252–260.

[73] S. De, A.P. Bartók, G. Csányi, M. Ceriotti, Comparing molecules and solids across structural and alchemical space, Phys. Chem. Chem. Phys. 18 (20) (2016) 13754–13769.

[74] B. Schölkopf, A. Smola, K.-R. Müller, Kernel principal component analysis, in: International Conference on Artificial Neural Networks, Springer, 1997, pp. 583–588.

[75] B.A. Helfrecht, R.K. Cersonsky, G. Fraux, M. Ceriotti, Structure-property maps with kernel principal covariates regression, Mach. Learn.: Sci. Technol. 1 (4) (2020) 045021.
[76] G.M. Torrie, J.P. Valleau, Nonphysical sampling distributions in Monte Carlo free-energy estimation: Umbrella sampling, J. Comput. Phys. 23 (2) (1977) 187–199.
[77] J. Kästner, Umbrella sampling, Wiley Interdiscipl. Rev.: Comput. Mol. Sci. 1 (6) (2011) 932–942.
[78] S. Börjesson, A. Emrén, C. Ekberg, A thermodynamic model for the calcium silicate hydrate gel, modelled as a non-ideal binary solid solution, Cem. Concr. Res. 27 (11) (1997) 1649–1657.
[79] J.M. Soler, Thermodynamic description of the solubility of CSH gels in hydrated portland cement. Literature review, 2007.
[80] J. Eikenberg, On the Problem of Silica Solubility at High pH, Tech. Rep., Paul Scherrer Inst. (PSI), 1990.
[81] K.R. Applin, The diffusion of dissolved silica in dilute aqueous solution, Geochim. Cosmochim. Acta 51 (8) (1987) 2147–2151.
[82] J. Haas, A. Nonat, From C–S–H to C–A–S–H: Experimental study and thermodynamic modelling, Cem. Concr. Res. 68 (2015) 124–138.
[83] C.S. Walker, S. Sutou, C. Oda, M. Mihara, A. Honda, Calcium silicate hydrate (C-S-H) gel solubility data and a discrete solid phase model at 25°C based on two binary non-ideal solid solutions, Cem. Concr. Res. 79 (2016) 1–30, http://dx.doi.org/10.1016/j.cemconres.2015.07.006, URL https://www.sciencedirect.com/science/article/pii/S0008884615001957.
[84] F.P. Glasser, E.E. Lachowski, D.E. Macphee, Compositional model for calcium silicate hydrate (C-S-H) gels, their solubilities, and free energies of formation, J. Am. Ceram. Soc. 70 (7) (1987) 481–485.
[85] M. Tanaka, K. Takahashi, The identification and characterization of silicate complexes in calcium chloride solution using fast atom bombardment mass spectrometry, Anal. Chim. Acta 411 (1–2) (2000) 109–119.
[86] M. Tanaka, K. Takahashi, Characterization of silicate monomer with sodium, calcium and strontium but not with lithium and magnesium ions by fast atom bombardment mass spectrometry, J. Mass Spectrom. 37 (6) (2002) 623–630.